The Shear-Bond Descriptor and Universal Machine-Learning Potential Enable Large-Scale Discovery of Negative Thermal Expansion Materials

Guangming Chen,[†,§] Shun Tian,[*,‡,†,§] Kaiwei Feng,[†] Yilun Liu,[‡] Wanjian Yin,[†] Qilong Gao,[*,¶] and Ke Zhou[*,†]

†*College of Energy, SIEMIS, Soochow University, Suzhou 215006, China*

‡ *Laboratory for Multiscale Mechanics and Medical Science, SV LAB, School of Aerospace, Xi'an Jiaotong University, Xi'an 710049, China*

¶*Key Laboratory of Materials Physics, Ministry of Education, School of Physics, Zhengzhou University, Zhengzhou 450001, China*

§*These authors contributed equally to this work.*

E-mail: tianshunxj@gmail.com; qilonggao@zzu.edu.cn; zhouke@suda.edu.cn

Abstract

Negative thermal expansion (NTE) materials are crucial for mitigating thermal stresses and designing dimensionally stable components in advanced technologies, yet compounds exhibiting this anomalous behavior remain intrinsically rare. The discovery of novel NTE crystals has traditionally relied on serendipitous empirical observation and physical intuition, severely hindered by the absence of universal design principles. Here, by integrating more than a century of accumulated thermal-expansion data with state-of-the-art machine learning, we identify explainable, macroscopic mechanical descriptors for thermal expansion, namely the shear modulus (G) and the bonding modulus ($\widetilde{E}$). These descriptors enable the construction of a universal thermal-expansion landscape based on the *shear-bond ratio* ($G/\widetilde{E}$), supporting robust classification between positive and negative thermal expansion materials across diverse structural and chemical spaces. Guided by these universal descriptors and powered by high-throughput, finite-temperature simulations using universal machine-learning interatomic potentials, we theoretically predict 3,665 NTE crystals exhibiting wide operating temperature windows. Validating this theory-driven paradigm, the experimental synthesis and characterization of 11 previously unreported compounds directly confirm the robust predictive power and transferability of our framework. These results bridge macroscopic mechanics with microscopic lattice dynamics, transforming the discovery of NTE materials into a systematic, scalable, and data-driven science.

Introduction

Thermal expansion is a fundamental property of solids, yet its behavior is remarkably asymmetric across materials.[1,2] Most materials exhibit positive thermal expansion (PTE), where the lattice expands upon heating due to the increased occupation of anharmonic phonon modes.[3] By contrast, a much smaller and structurally diverse subset exhibits negative thermal expansion (NTE), contracting as temperature increases.[4–6] NTE materials are of broad technological interest. Materials displaying NTE are essential for thermal-stress compensation and for realizing composites or devices with near-zero expansion, which enable dimensionally stable composites for precision optics and microelectronics and mitigate thermal stresses in aerospace and energy systems.[2,7–10] They also serve as key components in thermomechanical actuators where controlled contraction can be harnessed for motion or force generation.[11,12] Furthermore, the integration of NTE and PTE materials offers a versatile route to fabricate structures and devices through engineered thermal-expansion mismatch, enabling tunable curvature, adaptive architectures, and strain-programmable mechanical responses.[10,12–16]

Despite these wide-ranging applications, the fundamental principles governing why only certain materials contract upon heating remain incompletely understood, making systematic discovery a formidable challenge.[2,7–9] Historically, the search for NTE materials has relied heavily on empirical observation and physical intuition, largely confining discoveries to a small number of structural families known to host flexible or strongly anharmonic lattice motifs, such as framework oxides, zeolites, and cyanides.[7–9,17,18] While first-principles studies have elucidated key microscopic mechanisms of NTE,[8,19] their application remains largely limited to individual compounds or material classes, hindering systematic exploration of the vast chemical and structural space of crystalline solids. Consequently, NTE remains intrinsically rare, often confined to narrow temperature windows and specific crystal chemistries, with its strong coupling to elasticity and bonding further complicating rational materials design.[8] In contrast, more than a century of thermal-expansion measurements, together with rapidly expanding modern materials databases such as the Materials Project and GNoME, constitutes a rich yet underexploited data resource.[4,20,21] Fundamentally, the rarity of NTE reflects not a lack of data, but the absence of general, physically grounded descriptors that connect lattice dynamics, elasticity, and bonding across diverse materials.

Recent advances in artificial intelligence and data-driven materials science offer a powerful framework to extract such elusive principles from massive, heterogeneous datasets.[22–25] Previous ML studies have identified several useful structural and chemical factors for NTE discovery, including connectivity descriptors in open-framework oxides and fluorides, as well as average electronegativity and porosity in bulk framework materials.[26–28] These quantities have provided valuable empirical guidance for screening NTE candidates. Here, we demonstrate that the complex volume thermal expansion behavior of crystalline solids can be broadly understood and predicted using two universal mechanical descriptors, the shear modulus (G) and the *bonding modulus* ($\tilde{E}$). Rather than requiring computationally exhaustive microscopic phonon analyses, these macroscopic variables elegantly capture the physical competition between the negative and positive phonon contributions to thermal expansion. Together, they define a universal thermal-expansion landscape based on the *shear-bond ratio* ($\xi = G/\tilde{E}$), enabling robust and physically transparent classification of PTE and NTE materials across diverse material spaces. Interestingly, this shear-bond ratio maps thermal expansion from microscopic lattice dynamics to macroscopic mechanics, proving that expansion behavior is dictated simply by a material's relative stiffness against shape change versus volume change. By coupling this interpretable machine-learning descriptor with high-throughput, finite-temperature calculations powered by universal machine learning interatomic potentials (uMLIPs), we rapidly screen and identify over 6,000 novel NTE crystals. To rigorously validate this predictive framework, we synthesized and characterized 11 previously unreported compounds, confirming robust NTE behavior across a variety of structurally diverse chemistries. Ultimately, these results provide a general, interpretable, and scalable strategy that elevates the discovery of mechanically robust NTE materials from a process of empirical serendipity to one of systematic, data-driven design.

Results and Discussion

General physical picture of thermal expansion. NTE can arise from several distinct mechanisms, spanning phonon-mediated lattice dynamics, such as transverse vibrational modes and rigid-unit modes,[7,8,17,18] to electronic, magnetic, and spin-crossover transitions.[17,29,30] In this work, we focus on phonon-driven NTE because lattice-dynamic mechanisms represent the most prevalent and broadly applicable origin of NTE in crystalline solids.[7,8] In general, the thermal expansion coefficient (CTE, α) can be decomposed into positive and negative contributions as,

$$\alpha = \alpha^{+} + \alpha^{-} \tag{1}$$

where α^{+} and α^{-} denote the effective expansion and contraction contributions, respectively. This decomposition provides a general framework, provided that the relevant positive and negative contributions can be separated. For cubic crystals, this decomposition can be made more explicit within the Debye-Grüneisen theory.[19,31] The α can be expressed as the sum of contributions from phonon modes with positive and negative Grüneisen parameters (γ)

$$\alpha = \sum_{\gamma_{\boldsymbol{q}}} \alpha(\gamma_{\boldsymbol{q}}) = \sum_{\gamma_{\boldsymbol{q}}>0} \alpha(\gamma_{\boldsymbol{q}}) + \sum_{\gamma_{\boldsymbol{q}}<0} \alpha(\gamma_{\boldsymbol{q}}), \tag{2}$$

where $\alpha(\gamma_{\boldsymbol{q}})$ denotes the phonon-mode contribution to the overall thermal expansion. Materials exhibit NTE when the magnitude of the negative contribution (α^{-}) exceeds the positive one (α^{+}), i.e., when $|\alpha^{-}| > \alpha^{+}$ (or $|\alpha^{-}|/\alpha^{+} > 1$). Otherwise, they display PTE. This decomposition highlights that thermal expansion is governed by the competition between positive and negative phonon contributions. The positive term α^{+} arises from the intrinsic bond expansion with increasing temperature (see Fig. 1a),[22,32] whereas the negative term

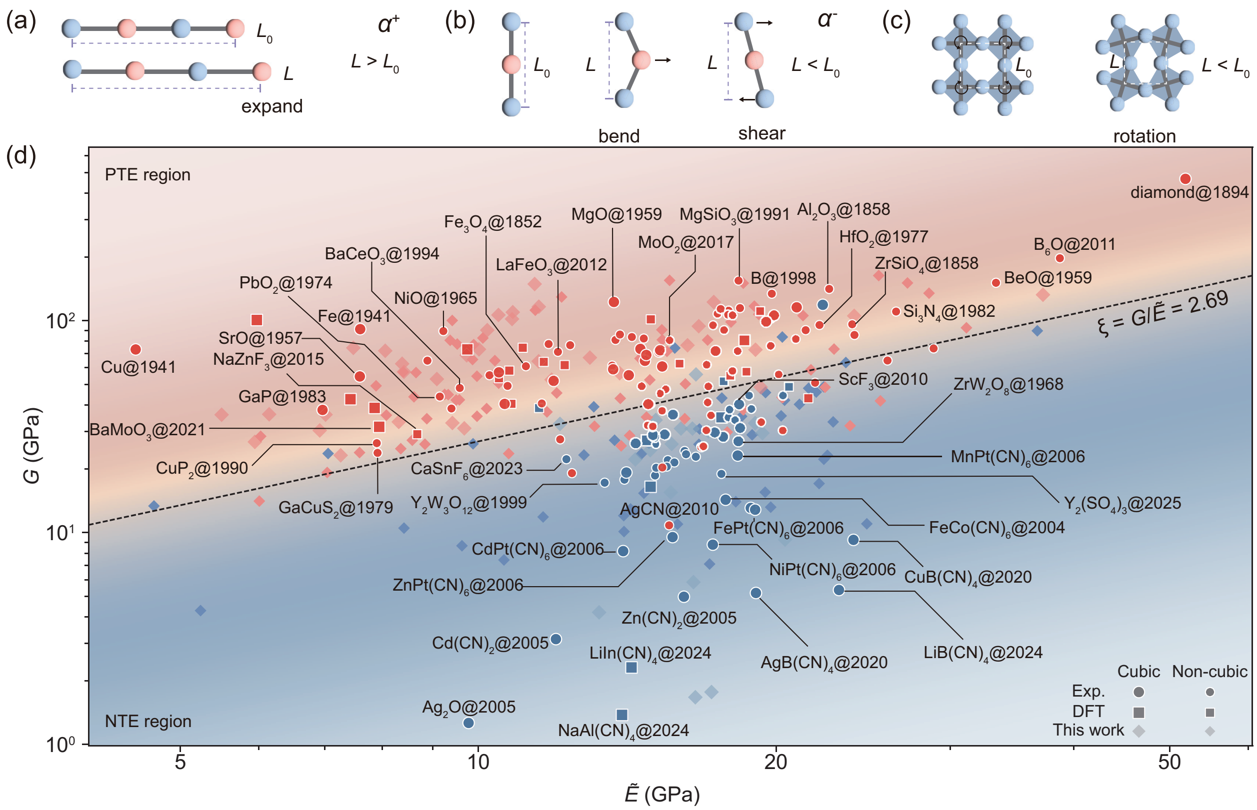

Figure 1: **Machine-learning-enabled, physically interpretable classification of PTE and NTE materials.** (a) The physical origin for the positive term α^+, which arises from the intrinsic bond expansion with increasing temperature. (b) The physical origin for the negative term α^-, which originates from low-frequency phonon modes involving collective shear, bending, or (c) rotational motions enabled by structural flexibility. (d) The positive/negative thermal expansion (PTE/NTE) classification map (shown on a logarithmic scale) is constructed using the shear modulus (G) and bonding modulus ($\widetilde{E}$). NTE materials are shown as blue points and PTE materials as red points; larger symbols denote cubic materials, whereas smaller symbols denote non-cubic materials. The classification boundary, $\xi_c = G/\widetilde{E} = 2.69$, was fitted using only the cubic materials and then applied without refitting to the non-cubic materials. Circles, squares, and diamonds denote experimentally reported materials, previously reported DFT results, and materials calculated in this work, respectively, and 44 points are labeled with their chemical formulas and years. Details of data selection and the full list of data points (Table S2) are provided in the **SI**. The labeled years indicate the cited experimental reports that explicitly characterized NTE, not necessarily the first discovery of each material.

α^- originates from low-frequency phonon modes involving collective shear, bending, or rotational motions enabled by structural flexibility (Figs. 1b, c).[7–9,17,18] The competition between these contributions provides the physical basis for exploring simple descriptors of volumetric thermal expansion in cubic crystals. However, translating these physical insights into simple, quantitative descriptors that enable scalable materials design and discovery remains a major challenge.

For non-cubic crystals, thermal expansion is intrinsically tensorial and generally follows $\alpha_i = V^{-1}\sum_j S_{ij}I_j$, with the off-diagonal compliance components coupling the directional responses and influencing the volumetric expansion (see details in **Methods**). This coupling makes the identification of a simple and physically interpretable descriptor more challenging than in cubic crystals, for which thermal expansion is isotropic by symmetry. We therefore first seek a descriptor using cubic crystals and subsequently evaluate its empirical transferability to non-cubic materials.

Machine learning descriptors and classification. To develop rational descriptors for thermal expansion and to enable reliable classification of PTE and NTE crystals, we integrate established physical knowledge to construct a set of physically meaningful features (see summary in Table S1). These features include quantities related to bonding characteristics (bulk modulus B, Young's modulus E, volumetric cohesive energy U_{V}), structural flexibility (shear modulus G, Poisson's ratio ν), structural attributes (average atomic volume $\widetilde{v_{\mathrm{A}}}$, average coordination number n, porosity ϕ), phonon-related information (Debye temperature Θ_{D}), and additional basic crystal descriptors (such as average electronegativity χ). Despite long-standing understanding of the physical origins of PTE and NTE (Figs. 1a–c), a general and quantitative descriptor for thermal expansion has remained elusive. Here, we employ the recently developed Sure Independence Screening and Sparsifying Operator (SISSO) method, a compressed sensing-based approach capable of generating predictive models and classification descriptors (see details in **Methods**).[25] Using SISSO, we trained classification models to distinguish PTE from NTE materials (see Figs. 1d, S1 and Table

S3). Our dataset spans more than a century (from 1852 to 2024), comprising 324 entries drawn from reported experimental measurements (134), prior DFT predictions (27), and 163 additional calculations performed in this work (see detailed information in Table S2). Together, these data provide broad and balanced coverage of chemical, structural, and physical space to mitigate sampling bias (see details in **SI** and Fig. S2). The 324 entries constitute the complete curated dataset used to characterize the chemical, structural, and physical coverage shown in Fig. S2. To avoid mixing the distinct thermal-expansion physics of cubic and non-cubic crystals, the dataset was subsequently partitioned according to crystal symmetry. Only the cubic subset, whose thermal expansion is isotropic by symmetry, was used for SISSO feature selection, model fitting, and determination of the classification boundary. The non-cubic subset was excluded from all model-training procedures and reserved exclusively for an external transferability test after the cubic model had been fixed.

Table S3 presents the mathematical formulas for the 9 best descriptors (ξ) selected from more than 1×10^6 candidates using the cubic subset (see the corresponding classification maps in Fig. S1). Among these, only descriptors that combine high predictive accuracy (high AUC) with low complexity (easy to compute) are suitable for guiding the discovery of new NTE materials. Dimensionless descriptors are particularly desirable due to their straightforward interpretability. Moreover, an effective descriptor should capture contributions from both positive and negative phonon modes that govern thermal expansion. In this context, we identify $\xi = G/(U_\mathrm{V}/n)$ as the most effective descriptor (Fig. 1d). Here, U_V represents the bonding strength per unit volume, while the coordination number n describes the number of nearest-neighbor bonds formed by each atom. Their ratio, U_V/n, therefore represents the cohesive-energy density distributed over the local bonding constraints, which can be interpreted as an effective macroscopic proxy for local bond stiffness (with units of GPa, see details in **SI**). We accordingly refer to this quantity as the *bonding modulus*, $\widetilde{E} = U_\mathrm{V}/n$, which is conceptually related to the concept of atomic stiffness.[33,34] Here, G serves as a macroscopic proxy for the shear flexibility associated with negative phonon contributions, whereas $\widetilde{E}$ represents the bond-stretching constraint associated with positive contributions. The resulting cubic-derived classification boundary is $\xi_c = G/\widetilde{E} = 2.69$, for which the classification accuracy reaches 97.03%. This shear-bond ratio (SBR) also correlates with the ratio $|\alpha^-|/\alpha^+$ within the cubic dataset (Fig. 2a), providing a quantitative measure of the competition between positive and negative phonon contributions in this symmetry class. Here, all PTE/NTE labels refer to the sign of the volumetric thermal expansion coefficient, rather than to directional linear expansion along a specific crystallographic axis. The shear modulus G is evaluated using the Voigt–Reuss–Hill averaging scheme, providing a consistent scalar measure of the overall shear resistance for descriptor construction.

After the descriptor and the boundary $\xi_c = 2.69$ had been fixed using only cubic crystals, they were applied without refitting to the non-cubic subset. The resulting classification accuracy is 83.17%, lower than the 97.03% obtained for the cubic dataset but still indicative of useful empirical transferability. This reduction also delineates the limitation of the scalar descriptor: it does not explicitly resolve the coupling between strain Grüneisen responses and individual off-diagonal components of the elastic compliance tensor in non-cubic crystals. Accordingly, for non-cubic materials, the SBR is used only as a prescreening metric, whereas their final thermal-expansion classification is determined using the strain-Grüneisen–compliance-tensor method described in the **Methods**.

The interpretation of mechanical descriptors. The descriptors obtained by the SISSO method offer distinct physical insights and are explainable. Within the isotropic approximation used to interpret the descriptor, the positive contribution, α^+ (see detailed derivation in **SI**), originates from anharmonic bond-stretching and longitudinal vibrational modes associated with the intrinsic asymmetry of interatomic potentials at finite temperature.[8] Based on a Morse-potential analysis of bond anharmonicity, the effective stiffness of these modes scales with the bonding modulus $\widetilde{E}$, an effective cohesive-energy density distributed over the local coordination environment. This leads to an inverse relationship between thermal expansion and bond strength, $|\alpha^+| \sim \widetilde{E}^{-1}$, in good agreement with our

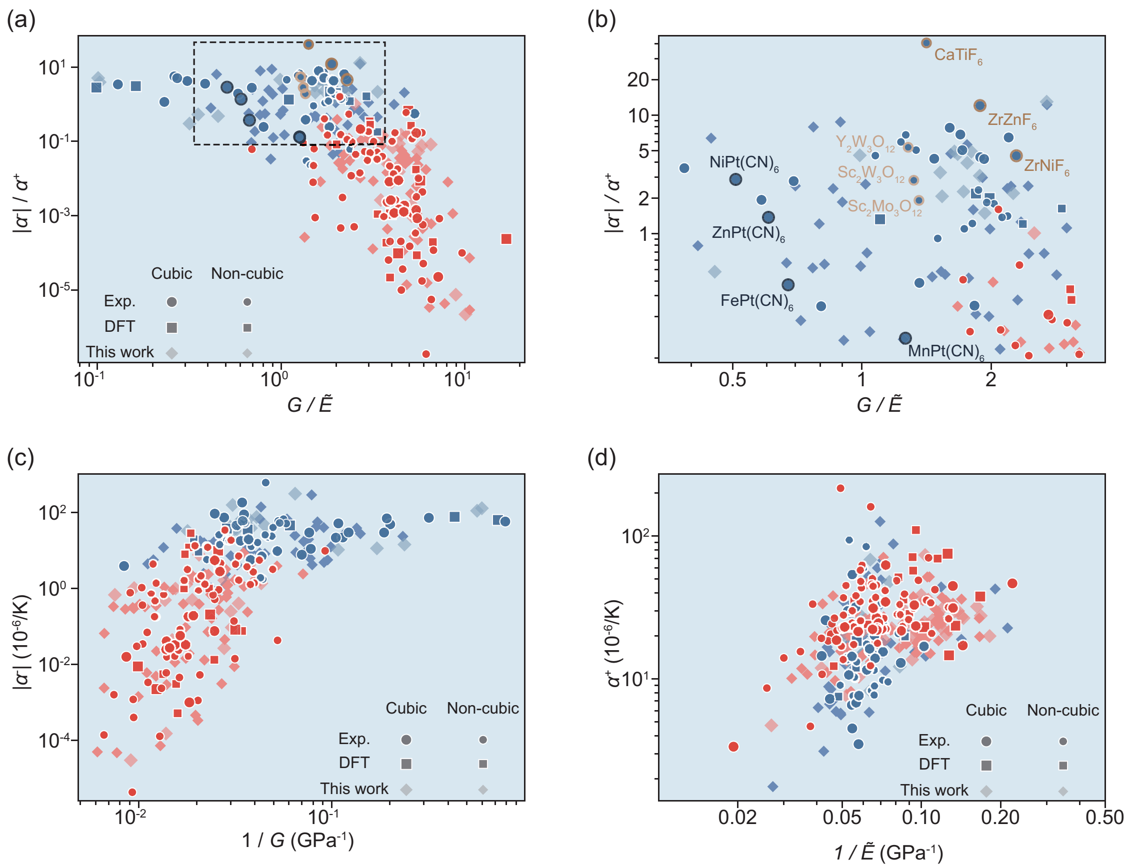

Figure 2: **Scaling relationships between macroscopic mechanical descriptors and microscopic thermal expansion components.** (a) The ratio of negative to positive thermal-expansion contributions ($|\alpha^-|/\alpha^+$) scales inversely with the shear-bond ratio ($\xi = G/\widetilde{E}$). (b) Enlarged view of the dashed region in (a), with representative materials in specific classes labeled. (c) The magnitude of the negative contribution ($|\alpha^-|$) exhibits an inverse scaling with the shear modulus (G), reflecting the role of structural shear flexibility. (d) The positive contribution (α^+) scales inversely with the bonding modulus ($\tilde{E}$), representing resistance to intrinsic bond expansion. In all panels, larger and smaller symbols denote cubic and non-cubic materials, respectively; circles, squares, and diamonds denote experimentally reported materials, previously reported DFT results, and materials calculated in this work, respectively. Blue and red points denote NTE and PTE materials, respectively.

calculations (Fig. 2d). In contrast, the negative contribution (α^-) is dominated by low-frequency transverse, shear, and rotational phonon modes that are characteristic of flexible open frameworks.[7,8,18,35] Framework lattice-dynamical theory shows that these modes contribute to thermal expansion with a weight proportional to $1/\omega^2$, and for shear-dominated modes the phonon frequencies satisfy $\omega^2 \sim G$, where G is the shear modulus and ω is the frequency of low-frequency transverse (shear-like) modes.[35] This directly leads to the scaling $|\alpha^-| \sim G^{-1}$, indicating that softer shear rigidity enhances the magnitude of the negative contribution, consistent with Fig. 2c. Combining these scaling relationships gives $\alpha^+/|\alpha^-| \sim G/\widetilde{E}$. Although this interpretation is derived from cubic crystals, both the cubic and non-cubic subsets exhibit similar overall scaling trends in Fig. 2, supporting the empirical transferability of the shear-bond ratio across crystal symmetries. The descriptor $G/\widetilde{E}$ naturally reflects the balance between rigid bond stretching and framework-like shear flexibility, providing a physically grounded explanation for its strong predictive power in distinguishing PTE and NTE materials. It should be emphasized that the present descriptor is designed as a binary classifier for the sign of α, rather than as a quantitative predictor of the absolute value of $\alpha(T)$. Therefore, proximity to the classification boundary should not be interpreted as zero thermal expansion (ZTE). Extending this framework to ZTE discovery would require redefining the learning target as a temperature-specific or window-averaged α, using either regression or multi-class PTE/NTE/ZTE classification.

It is important to note that while thermal expansion is intrinsically an anharmonic phenomenon, the macroscopic manifestation of these anharmonic structural distortions is heavily constrained by the lattice's harmonic restoring forces. Consequently, rather than contradicting the anharmonic nature of thermal expansion, the harmonic mechanical descriptors (G and $\widetilde{E}$) effectively serve as *scaling factors* associated with the relative excitation weights and amplitudes of the competing positive and negative anharmonic phonon modes. This conceptual abstraction closely parallels the historical significance of Pugh's ratio (B/G), which famously mapped the microscopic complexities of dislocation dynamics into a simple macroscopic predictor for ductility and brittleness.[36] Crucially, the SBR is a macroscopic mechanical descriptor rather than a microscopic lattice-dynamical one. It reveals an important statistical and physical insight: although thermal expansion is ultimately governed by complex microscopic lattice dynamics, the resulting behavior correlates strongly with the material's relative stiffness in resisting shape change versus resisting bond-stretching deformation. The persistence of this trend across cubic and non-cubic crystals does not imply an identical microscopic mechanism, but rather a coarse-grained mechanical regularity. The quantities G and $\widetilde{E}$ characterize the competing energy scales of transverse/shear deformation and bond stretching, respectively, both of which remain relevant across crystal symmetries. In non-cubic crystals, strain Grüneisen responses and off-diagonal elastic-compliance components reweight these tendencies, reducing the classification accuracy without eliminating the overall trend. Thus, $G/\widetilde{E}$ provides a transferable scalar indicator of thermal-expansion propensity, while the tensorial coupling supplies the symmetry-dependent information required for final evaluation.

Although the descriptor $G/\widetilde{E}$ is similar to Pugh's ratio, our calculations show that their values exhibit no apparent correlation (Fig. S3), confirming that ξ captures a uniquely distinct thermomechanical balance rather than a general elastic property. Previously reported descriptors such as porosity, connectivity, and electronegativity are related to the present descriptor.[26–28] Rather, they can be understood as structural or chemical factors that modulate the underlying mechanical quantities G and $\widetilde{E}$. The shear-bond descriptor therefore captures these structural and chemical effects through the more fundamental mechanical quantities G and $\widetilde{E}$. The remaining deviations, particularly among non-cubic materials, reflect physical contributions not explicitly resolved by this scalar descriptor, including anisotropic elastic coupling, low-frequency optic modes, and temperature- or pressure-dependent changes in bonding and coordination.[7,8,29]

The discovery of thousands of NTE materials using uMLIPs. Guided by the physically interpretable shear-bonding ratio descriptor, we performed a large-scale search

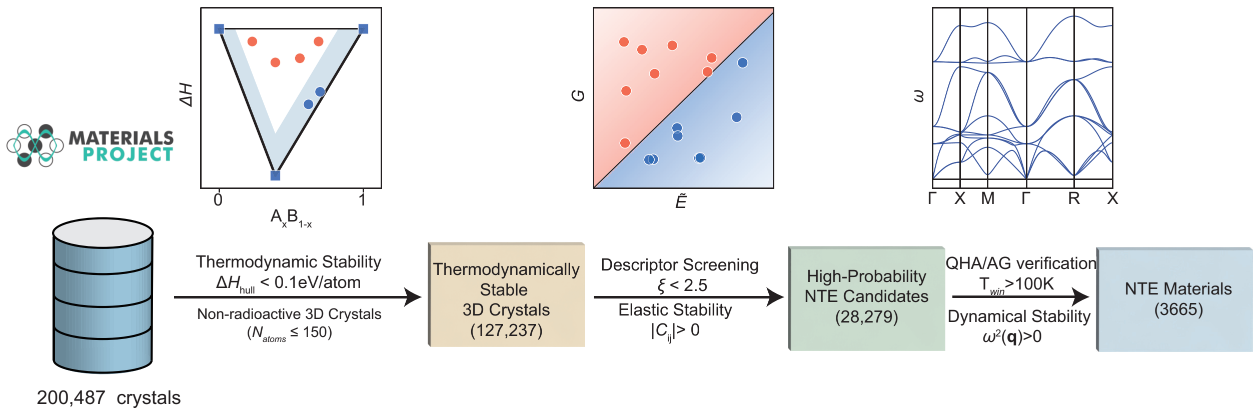

Figure 3: **High-throughput data-driven discovery workflow for NTE materials.** Starting with over 200,000 non-radioactive 3D crystals from the Materials Project database, the screening pipeline sequentially applies filters for thermodynamic stability ($\Delta H < 0.1$ eV/atom) and elastic stability. Materials are then screened using the macroscopic mechanical criterion ($\xi < 2.5$) to identify high-probability NTE candidates. In the final screening step, phonon-stability screening, QHA/AG validation (AG denotes the anisotropic Grüneisen method), and thermal-expansion screening are performed. The cubic (isotropic) materials are evaluated using QHA, whereas non-cubic (anisotropic) materials are evaluated using AG (see details in **Methods**). The complete library is available in the open-access NTEdb.[37]

for NTE materials across the Materials Project database.[20] Starting from over 200,000 non-radioactive three-dimensional crystalline compounds, successive filters based on thermodynamic stability, elastic stability, and the conservative descriptor criterion ($\xi < 2.5$) rapidly reduced the search space to a high-probability NTE subset (Fig. 3). To further validate these candidates beyond static mechanical descriptors, we evaluated temperature-dependent thermal expansion in a final symmetry-resolved stage that combined phonon-stability screening with thermal-expansion calculations: cubic materials were evaluated using isotropic QHA, whereas non-cubic materials were evaluated using the anisotropic Grüneisen method (see details in **Methods**). These calculations were enabled by uMLIPs, which provide near first-principles accuracy at a computational cost compatible with high-throughput screening, providing 100 to 1000-fold speedup relative to density functional theory calculations. Recent studies have shown that uMLIPs are now sufficiently accurate for phonon calculations,[38,39] and very recent work further demonstrates the ability of MatterSim to predict thermal conductivity, which requires accurate third- and higher-order force constants.[39] By contrast, thermal expansion depends primarily on second-order force constants, placing it well within the reliable regime of the model. We emphasize that the central task of this work is to determine the sign of volumetric thermal expansion, namely PTE versus NTE, rather than to quantitatively reproduce the exact magnitude of $\alpha(T)$ (see details in **SI**). To validate this use, we benchmarked MatterSim-based QHA against DFT calculations for 18 representative cubic materials (Figs. S4 and S5). The results show that MatterSim qualitatively reproduces $\alpha(T)$ and reliably determines the sign of α. It is further supported by the agreement in the sign of the macroscopic Grüneisen parameter $\bar{\gamma}(T)$ (Figs. S6 and S7), which directly controls the PTE/NTE sign within the QHA framework. For the non-cubic branch, anisotropic Grüneisen calculations for 18 materials spanning six crystal systems reproduce the principal directional and volumetric temperature-dependent trends reported in the literature (Figs. S8 and S9). Through this combined descriptor-based and symmetry-resolved finite-temperature validation workflow, we identify thousands of NTE materials exhibiting stable negative thermal expansion over temperature windows (T_w) exceeding 100 K. We further establish a large, physics-guided, and provenance-tracked NTE materials database (NTEdb), available at NTEdb.com.[37] Importantly, the scale of discovery is achieved without sacrificing physical interpretability, underscoring that the descriptor, not the computational method, constitutes the central advance of this work.

Experimental validation. To validate the physically interpretable classification model, we synthesized 11 previously unreported NTE materials spanning oxide and fluoride chemistries (Table 1). Five materials were selected directly from the predicted NTE library (marked with $\star$), while additional quaternary and five-element compounds (6 materials) that are absent from the MP database were prepared to assess model transferability beyond existing datasets. All candidates were selected based on synthesis feasibility while deliberately sampling diverse chemistries and crystal structures to minimize selection bias. Detailed synthesis procedures and characterization methods are provided in the **SI**. Fig. 4 presents two representative examples (the results of average α in NTE windows for other materials are

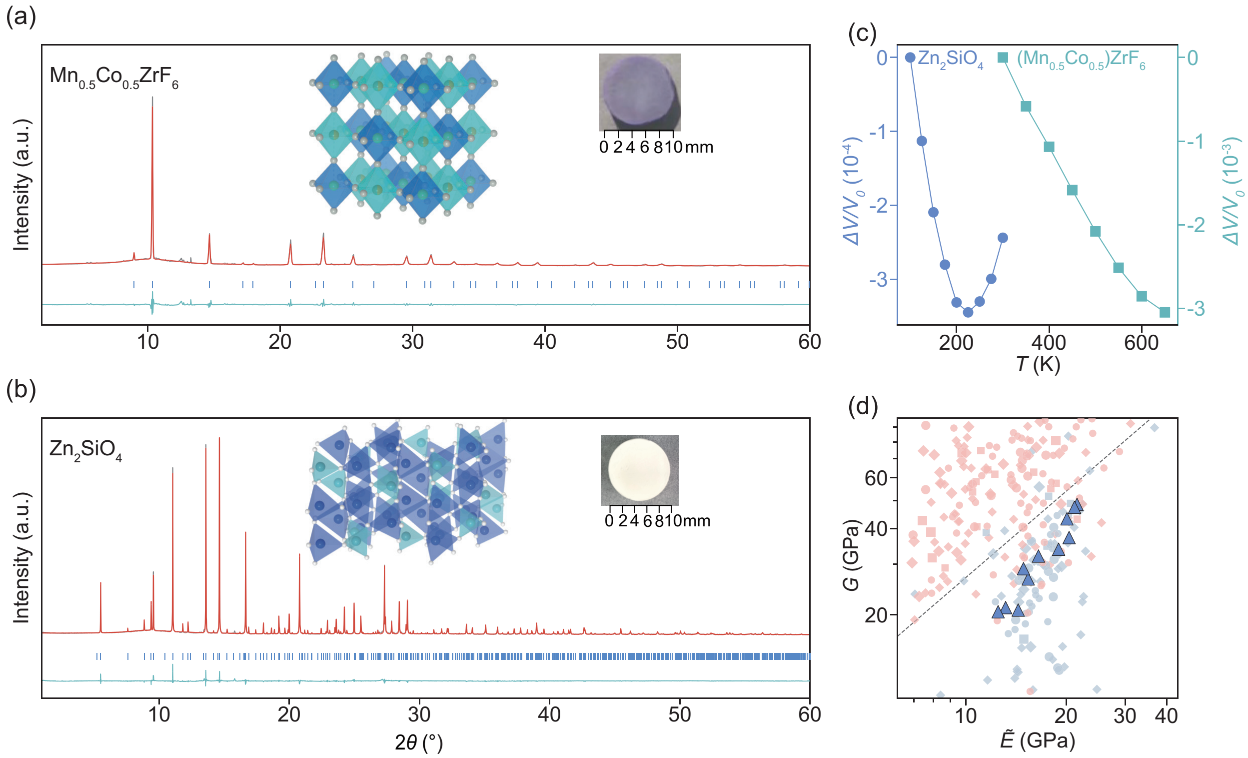

Figure 4: **Experimental realization and validation of predicted NTE materials.** (a) Rietveld refinements using synchrotron X-ray diffraction (SXRD) data for $Mn_{0.5}Co_{0.5}ZrF_6$ and (b) Zn_2SiO_4 at 300 K. The plots display the measured X-ray diffraction profiles (red dots), the theoretical fit (black line), and the difference between the two (teal line). Vertical ticks (dark blue) indicate the Bragg peak positions. The insets show the corresponding crystal structures and optical images of the synthesized samples. (c) Temperature-dependent relative volume changes ($\Delta V/V_0$) derived from variable-temperature XRD. Data for Zn_2SiO_4 (dark blue circles) and $(Mn_{0.5}Co_{0.5})ZrF_6$ (teal squares) are plotted on the left and right axes, respectively. (d) The location of the 11 previously unreported NTE materials (teal triangles) synthesized in this work plotted on the classification model.

shown in Table 1). The fluoride $Mn_{0.5}Co_{0.5}ZrF_6$ (MCZF) crystallizes in a cubic framework of alternating Mn/CoF_6 and ZrF_6 octahedra, as confirmed by Rietveld refinements using synchrotron X-ray diffraction (SXRD) data. High-temperature diffraction reveals pronounced isotropic NTE with $\alpha = -8.73 \times 10^{-6}\,\mathrm{K}^{-1}$ between 300 and 650 K, originating from transverse vibrational modes of fluorine atoms.[7,8] In contrast, Zn_2SiO_4 (ZSO) exhibits weaker NTE ($\alpha = -2.76 \times 10^{-6}\,\mathrm{K}^{-1}$, 100–225 K). Its framework structure, resolved by combined neutron and synchrotron diffraction, consists of interconnected SiO_4 and ZnO_4 tetrahedra forming mixed-membered rings with two-coordinated oxygen atoms, distinct from classical

Table 1: **Summary of 11 previously unreported NTE materials synthesized in this work.** Materials marked with a star are selected directly from the predicted NTE library. The remaining quaternary and five-element compounds (6 candidates) are absent from the MP database and were synthesized to assess the transferability of the model beyond existing datasets. The table lists their calculated shear modulus (G), bonding modulus ($\tilde{E}$), the resulting shear-bond ratio (ξ), and the average thermal expansion coefficients ($\bar{\alpha}$) within their NTE temperature windows, all of which correctly predicted their experimentally confirmed NTE behavior.

No.	Materials	G	$\widetilde{E}$	ξ	$\overline{\alpha}$	NTE/PTE
1	$BaCrSi_4O_{10}$ ⋆	33.837	18.974	1.783	-4.12	NTE
2	$CaCuSi_4O_{10}$ ⋆	48.473	21.540	2.250	-3.62	NTE
3	$SrCuSi_4O_{10}$ ⋆	37.153	20.398	1.821	-3.87	NTE
4	$CuZnV_2O_7$ ⋆	26.683	15.386	1.734	-6.83	NTE
5	Zn_2SiO_4 ⋆	32.039	16.516	1.940	-2.76	NTE
6	$Mn_{0.5}Co_{0.5}ZrF_6$	20.779	14.362	1.447	-8.73	NTE
7	$BiZr_6P_9O_{36}$	43.184	20.093	2.149	-10.20	NTE
8	$EuHf_6P_9O_{36}$	47.347	21.174	2.236	-3.50	NTE
9	$Zn_2Ge_{0.5}Si_{0.5}O_4$	28.954	14.895	1.944	-3.33	NTE
10	$K_{0.5}Co_{0.5}Sc_{1.5}Mo_3O_{12}$	21.196	13.170	1.609	-8.72	NTE
11	$K_{0.5}Zn_{0.5}Sc_{1.5}Mo_3O_{12}$	20.495	12.508	1.639	-10.70	NTE

NTE oxides such as ZrW_2O_8.[5] Despite their structural and chemical diversity of these 11 NTE materials, all synthesized compounds lie within the predicted NTE region (Fig. 4d), providing direct experimental validation of the model.

All 11 phase-pure candidates characterized by variable-temperature XRD exhibited the predicted NTE behavior, corresponding to a 100% success rate for the property-prediction component of our workflow. This result supports the reliability of the physically interpretable shear-bond descriptor combined with uMLIP/QHA validation. We note that the predicted library of 3,665 NTE materials represents a physics-guided candidate pool, rather than a guaranteed list of readily synthesizable compounds, because synthesis kinetics and competing phase formation are not explicitly considered.

Structural-Chemical Origins of the NTE Landscape. The discovered NTE materials can be further analyzed through a structural-chemical decomposition. Specifically, the predicted NTE materials can be classified according to their backbone-cation frameworks and dominant local anionic motifs. As shown in Fig. 5a, ξ exhibits a strong statistical dependence on the topological connectivity of these microscopic polyhedral backbones. As the structural topology evolves from zero-dimensional (0D) isolated polyhedra or 1D chains (1D-C) to 2D connected or fully connected three-dimensional corner-sharing (2D-CS, 3D-CS) frameworks, the group medians generally shift toward the high-modulus region along iso-ξ lines. This topological evolution elucidates the central physical trade-off in NTE design: low-dimensional backbones, lacking rigid inter-polyhedral constraints, exhibit a severely softened G. This softening releases substantial transverse vibrational degrees of freedom, facilitating enhanced NTE contributions. In contrast, 3D-CS networks leverage hinge-like flexibility at the vertices to sustain NTE while preserving high $\tilde{E}$. The darker CTE of some 3D-CS subgroups further indicates that connectivity alone does not uniquely determine the thermal-expansion magnitude. This association is consistent with a contribution from weakened shear rigidity in low-dimensional topological frameworks, which can amplify transverse and rotational lattice motions that generate NTE contributions. Although the present analysis focuses on three-dimensional bulk crystals, this physical picture is consistent with the well-known occurrence of NTE in low-dimensional systems, such as 1D atomic chains and 2D monolayer materials, where the resistance to transverse shear or out-of-plane deformation is intrinsically weak.[22,40] This suggests a common mechanical tendency in which reduced shear or transverse rigidity can amplify transverse and rotational lattice motions that generate NTE contributions.

To translate this macroscopic descriptor into chemical guidelines, Fig. 5b presents a chemistry-resolved heatmap that categorizes the NTE dataset by dominant local anionic motifs (rows) and backbone-cation classes (columns). Although this representation does not include special cases that lack a distinct backbone cation, such as pure framework oxides like $Ba_2Si_3O_8$, it captures the broad chemical diversity of the predicted NTE library. Notably, the heatmap exhibits a predominantly horizontal pattern within the populated cells. The materials sharing the same local anionic motif generally show similar median ξ values across

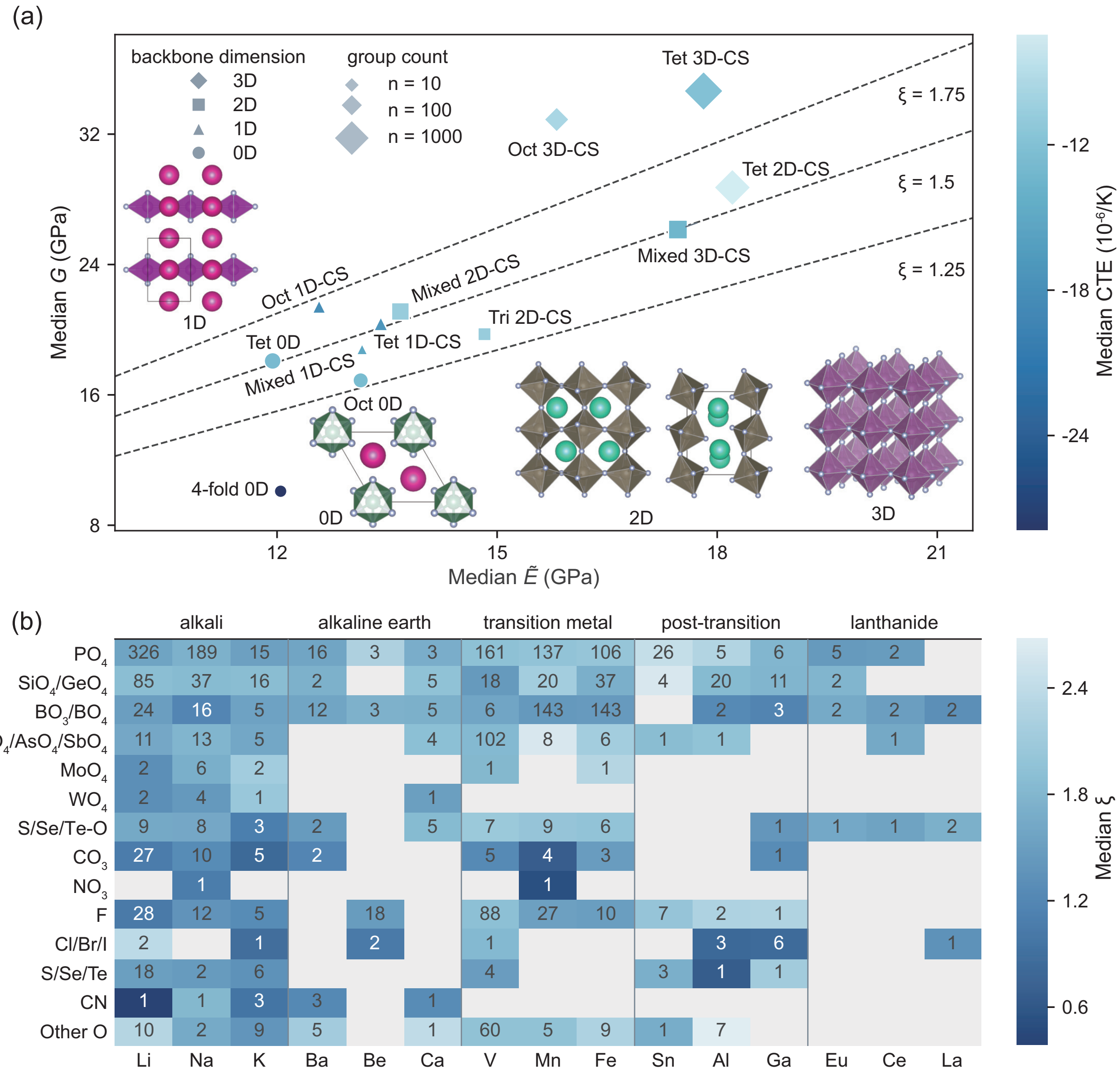

Figure 5: **Topology- and motif-resolved organization of the NTE shear-bond landscape.** (a) Median G versus $\widetilde{E}$ for representative backbone-topology groups within the classified NTE dataset. Group labels indicate the dominant polyhedral geometry, spatial dimension, and connectivity of the backbone; for instance, Tet 2D-CS represents a tetrahedral two-dimensional corner-sharing network, while Tet 0D denotes isolated tetrahedral units. The shape, size, and color of the markers correspond to the backbone dimension, group population size, and median volume coefficient of thermal expansion (CTE), respectively. Dashed lines ($\xi = 1.25, 1.50$, and 1.75) are provided for reference. (b) Median ξ values mapped across dominant local anionic motif families (rows) and representative backbone-cation elements (columns). The columns are further categorized by backbone-cation class along the top horizontal axis. The color intensity of each cell reflects the median ξ, while the numerical value indicates the sample count. Blank cells denote motif-cation combinations that are absent from the present classified NTE dataset.

different backbone-cation classes, whereas changing the motif generally leads to a larger shift in ξ. This observation suggests that the dominant local anionic motif provides the primary chemical organization of ξ, while backbone-cation identity introduces additional within-family variation.

To examine the mechanical origin of these motif-dependent trends, Fig. 6a projects the statistical distribution of motif families onto the macroscopic G-$\widetilde{E}$ landscape. This representation reveals that different chemical motifs reach the low-ξ regime through distinct elastic trade-offs. Halides (Cl/Br/I), for instance, approach the low-ξ regime via proportional softening, simultaneously depressing both the shear and bonding moduli. In contrast, cyanides (CN) and nitrates (NO_3) deviate from this proportional trend by reducing G while retaining comparatively larger $\widetilde{E}$ in the present grouped medians, thereby producing pronounced shear-bond asymmetry. Conversely, phosphate-based motifs (PO_4), which constitute the largest sub-population in the dataset, commonly populate an intermediate-ξ regime, providing a mechanically robust compromise between lattice contraction and framework stiffness.

Transferability of the Shear-Bond Descriptor. Importantly, the applicability of the SBR descriptor beyond conventional inorganic crystals was further examined using literature-reported thermal-expansion data for polymers, van der Waals molecular crystals, metal-organic frameworks (MOFs), zeolites, and amorphous materials (Fig. 6b). It should be noted that the PTE/NTE labels for these extended material classes were not obtained from Debye-Grüneisen calculations in this work. Rather, they were taken from previously reported experimental measurements or, for a small number of MOFs, molecular-dynamics simulations. Despite the distinct microscopic origins of thermal expansion in these systems, the SBR descriptor still provides a consistent macroscopic separation between reported PTE and NTE behavior. This observation suggests that the competition between overall shear flexibility and bond stiffness captures a transferable mechanical tendency associated with thermal expansion, while quantitative prediction of thermal expansion in soft or highly flexible materials requires more specialized methods. Therefore, Fig. 6b should be viewed as

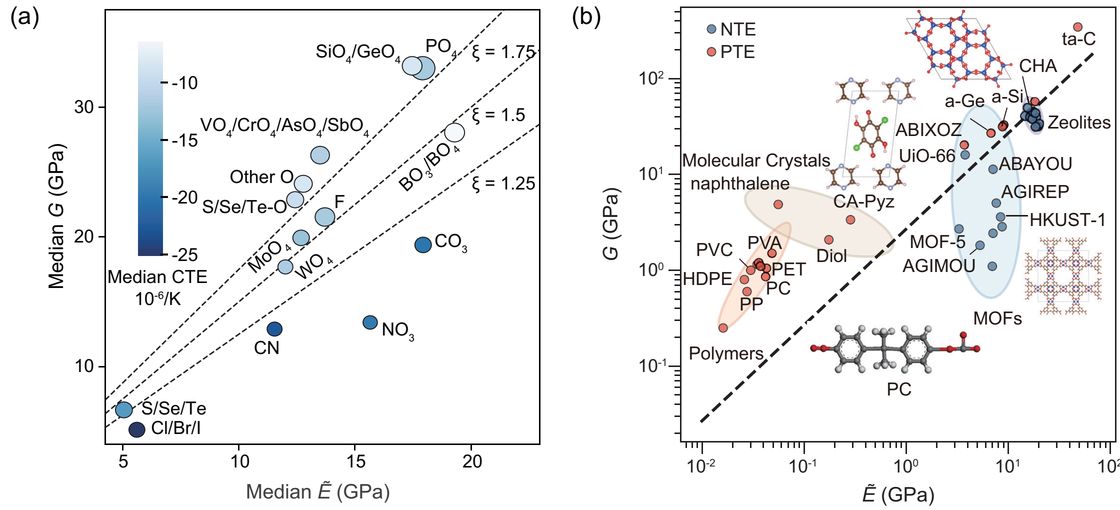

Figure 6: **Motif-family routes to low ξ and transferability of the macroscopic classification boundary.** (a) Distribution of the median properties for dominant local motif families across the macroscopic G-$\widetilde{E}$ plane. Marker size is proportional to the number of materials in each family, and color denotes the median CTE. Dashed lines ($\xi = 1.25$, 1.50, and 1.75) are shown for reference. (b) Extension of the macroscopic classification model beyond conventional inorganic crystals. The cubic-derived classification boundary ($\xi_c = G/\widetilde{E} = 2.69$, dashed line) accurately delineates the PTE (red) and NTE (blue) regimes for fundamentally diverse material classes, including polymers, van der Waals molecular crystals, metal-organic frameworks (MOFs), zeolites, and amorphous networks. Details of the calculations of G and $\widetilde{E}$ are shown in the **SI** and Tables S4–S6.

an additional transferability test of the descriptor, rather than as a Debye-Grüneisen-based prediction for these material classes.

Scope, Limitations, and Outlook.

Extending the Positive-Negative Contribution Framework. More broadly, the decomposition $\alpha = \alpha^+ + \alpha^-$ can be viewed as a general framework for thermal expansion beyond phonon-driven NTE. For phase-transition-driven NTE, α^- may originate from transition-induced strain, such as volume collapse, framework tilting, or ferroelastic distortion, while α^+ represents the normal phonon background.[7] In such cases, descriptors should include order-parameter-strain coupling, transition temperature, and elastic stiffness. In particular, G may remain important when the transition involves shear distortion. For magnetic or electronic NTE, α^- may arise from magnetovolume coupling, spin-state changes, charge transfer, or electronic instabilities, suggesting that magnetic, electronic, and electron-lattice-coupling descriptors are needed.[7,29] Thus, while the present shear-bond descriptor is developed for fixed-phase phonon-driven NTE, the same positive-negative contribution framework provides a possible route to unify broader NTE mechanisms.

Conclusion

Here we present a scalable and physically grounded approach for predicting and discovering NTE materials across the crystalline materials landscape by combining historical thermal-expansion data with state-of-the-art machine-learning methods. Our analysis identifies two universal mechanical descriptors, the shear modulus G and the bonding modulus $\widetilde{E}$, that quantitatively capture the competition between negative and positive phonon contributions to thermal expansion. These descriptors enable robust classification of PTE and NTE materials across broad chemical and structural spaces. By integrating this descriptor-based classification model with high-throughput finite-temperature simulations using uMLIPs, we predict 3,665 NTE materials. The significance of this massive library lies not merely in enlarging the list of known NTE compounds, but in providing a searchable design space for thermal-expansion engineering. This resource supports multi-objective selection under critical engineering constraints, such as operating temperature windows and mechanical stiffness, thereby enabling scalable zero-expansion solutions and programmable thermally induced shape change. Importantly, the successful experimental realization of 11 structurally diverse, previously unreported NTE materials provides compelling validation of the physically interpretable descriptors and underscores their utility for scalable, data-driven materials discovery. This work establishes a general strategy for data-driven yet physically transparent materials discovery, demonstrating that complex anharmonic properties such as thermal expansion can be efficiently navigated at scale. While our focus here is on phonon-driven thermal expansion, the same strategy is readily extendable to electronic- and spin-driven mechanisms as machine-learning models of electronic and magnetic excitations continue to advance.[41–43]

Methods

Isotropic QHA calculations. Temperature-dependent volumetric thermal expansion coefficients, $\alpha(T)$, for cubic materials were evaluated within the QHA as implemented in the Phonopy package.[44] For cubic crystals, the thermal-expansion tensor is isotropic by symmetry, so the volumetric response can be obtained from a uniform volume coordinate without resolving independent directional strains. For each material, the relaxed structure was used to generate volume-dependent configurations and phonon spectra. At each volume, the corresponding static energy and phonon frequencies were combined to evaluate the Helmholtz free energy as $F(V,T) = E_0(V) + F_{\mathrm{vib}}(V,T)$, where $F_{\mathrm{vib}}(V,T) = \sum_{\mathbf{q}\nu}\left[\frac{1}{2}\hbar\omega_{\mathbf{q}\nu}(V) + k_{\mathrm{B}}T\ln\left(1-\exp\left[-\frac{\hbar\omega_{\mathbf{q}\nu}(V)}{k_{\mathrm{B}}T}\right]\right)\right]$. Here, $E_0(V)$ is the static energy at volume V, while $F_{\mathrm{vib}}(V,T)$ contains the zero-point and thermal vibrational contributions. The volume dependence of $\omega_{\mathbf{q}\nu}(V)$ therefore provides the quasiharmonic thermal pressure. The equilibrium volume at each temperature was obtained by minimizing $F(V,T)$ with respect to volume, equivalently satisfying $\left.\frac{\partial F(V,T)}{\partial V}\right|_{V=V(T)} = 0$. The volumetric coefficient was then calculated from the temperature derivative of the equilibrium volume as $\alpha(T) = V(T)^{-1}\mathrm{d}V(T)/\mathrm{d}T$. The sign of $\alpha(T)$ was used to distinguish PTE from NTE in the cubic branch. In the cubic limit, this scalar result is equivalent to the trace of the tensorial treatment below, with $\alpha = 3\alpha_{\mathrm{lin}}$.

Anisotropic Grüneisen–elasticity calculations.

For non-cubic crystals, temperature-dependent thermal expansion was evaluated with the anisotropic Grüneisen–elasticity (AG) method, which combines strain-resolved phonon responses with the full elastic compliance tensor.[28,31,45] Starting from a relaxed structure, independent finite strains were applied to the equilibrium cell, and the phonon spectrum was recalculated for each strained configuration. In compact strain-component notation, the mode Grüneisen responses, their heat-capacity-weighted driving terms, and the resulting expansion components were evaluated as $\gamma_{\mathbf{q}\nu}^{(j)} = -\frac{\partial \ln \omega_{\mathbf{q}\nu}}{\partial \eta_j}\Big|_{\boldsymbol{\eta}=0}$, $I_j(T) = \frac{\sum_{\mathbf{q}\nu} w_{\mathbf{q}} c_{\mathbf{q}\nu}(T)\gamma_{\mathbf{q}\nu}^{(j)}}{\sum_{\mathbf{q}} w_{\mathbf{q}}}$, and $\alpha_i(T) = \frac{1}{V_0}\sum_j S_{ij} I_j(T)$. Here, $\omega_{\mathbf{q}\nu}$ denotes the frequency of mode $(\mathbf{q}, \nu)$, $c_{\mathbf{q}\nu}(T)$ is its mode heat capacity, and $w_{\mathbf{q}}$ is the q-point weight. The indices i and j refer to the same independent strain components, V_0 is the equilibrium volume, and S_{ij} is the corresponding full elastic compliance tensor. The first relation was evaluated from finite differences of the phonon frequencies of the strained configurations. At each temperature, the heat-capacity weighting in $I_j(T)$ accounts for the thermal population of the modes, while contraction with S_{ij} retains the coupling between normal and shear responses. The resulting components were assembled into a Cartesian thermal-expansion tensor. Unlike a scalar volume derivative, this tensorial treatment allows the response to differ along the crystallographic directions. Directional coefficients were obtained by projecting the tensor onto the corresponding crystallographic axes, while the volumetric coefficient was obtained from its trace, $\alpha(T) = \mathrm{Tr}[\boldsymbol{\alpha}(T)]$. The sign used for the volumetric NTE/PTE label was therefore the sign of this traced coefficient, rather than that of any single directional component, so compensating positive and negative directional responses are retained in the volumetric classification. For cubic crystals, symmetry makes the expansion tensor isotropic, and the AG formulation reduces to the scalar QHA result above, with $\alpha = 3\alpha_{\mathrm{lin}}$.

Details about DFT and uMLIP calculations. High-throughput screening and property calculations were primarily performed using the universal machine-learning interatomic potential MatterSim.[46] Two model variants were employed to balance efficiency and accuracy: MatterSim-1M was used for derivative-sensitive calculations, including phonon spectra and elastic constants, due to its robust force predictions and computational efficiency, while MatterSim-5M was used for static total-energy evaluations associated with cohesive energy calculations, where higher accuracy in absolute energies is required. Structural relaxations and phonon calculations were performed consistently with the MatterSim potential. To validate the reliability of the machine-learning predictions, representative NTE candidates were further examined using density functional theory (DFT) calculations. DFT calculations were performed using the Vienna Ab initio Simulation Package (VASP)[47,48] with the projector augmented wave (PAW) method[49] and the Perdew-Burke-Ernzerhof (PBE) generalized gradient approximation functional.[50] The corresponding computational details are provided in the Supplementary Information.

Calculation of mechanical properties and scalar descriptors. Two mechanical descriptors were considered in this work: the shear modulus (G) and the bonding modulus ($\tilde{E}$). Elastic constants were obtained using the energy–strain approach implemented with VASPKIT.[51] Total energies were evaluated with the MatterSim-1M model,[46] and the elastic stiffness tensor (C_{ij}) was extracted by fitting the energy–strain relations. Its inverse was retained as the full compliance tensor (S_{ij}) for the anisotropic calculations, while the scalar shear modulus (G) used in the descriptor was computed using the Voigt–Reuss–Hill averaging scheme. Thus, the VRH average provides a scalar measure for descriptor construction and prescreening, whereas the full tensor is used for the non-cubic thermal-expansion response. The bonding modulus was defined as $\tilde{E} = U_V/n$, where U_V is the volumetric cohesive energy density and n is the average coordination number. This normalization accounts for variations in local bonding environments and yields a transferable measure of bond stiffness. Coordination numbers were determined using the CrystalNN algorithm[52] implemented in pymatgen,[53] employing the default unweighted Voronoi-based neighbor-finding scheme. The average coordination number was obtained by averaging over all atoms in the unit cell. The volumetric cohesive energy density was calculated as, $U_V = (E_{\text{total}} - \sum_i N_i E_{\text{isolated},i})/V_{\text{cell}} \times C$, where E_{total} is the total energy of the unit cell evaluated using the MatterSim-5M model, V_{cell} is the unit-cell volume, and $C = 160.217$ converts eV/Å^3 to GPa. To ensure consistency with experimentally reported cohesive energies, the reference energy of isolated atoms was obtained via a thermodynamic cycle: $E_{\text{isolated}} = E_{\text{bulk}}^{\text{MP}} + E_{\text{coh}}^{\text{exp}}$. Here, $E_{\text{bulk}}^{\text{MP}}$ is the ground-state energy of the elemental solid from the Materials Project,[20] and $E_{\text{coh}}^{\text{exp}}$ is the experimental cohesive energy compiled by Kittel.[54] Since $\tilde{E}$ is used as a relative descriptor, the analysis is insensitive to a uniform shift in absolute reference energies.

Cubic-only SISSO classification. To identify the interpretable physical descriptors governing the sign of thermal expansion, we employed the SISSO method.[25] The dataset comprised 324 materials. The SISSO training domain comprised 109 cubic materials (48 NTE and 61 PTE), while 215 non-cubic materials (69 NTE and 146 PTE) were held out as out-of-domain (OOD) diagnostics and were not used for feature selection, model fitting, or determination of the classification boundary. Based on the sign of their volumetric thermal expansion coefficients at 100 K (with NTE defined by an NTE window $T_{\mathrm{w}} > 100$ K), these 324 materials were categorized into 117 NTE and 207 PTE entries. The selection of 100 K as the evaluation reference is physically motivated. At this temperature, the low-frequency transverse and shear phonon modes responsible for NTE are typically fully activated, while the high-frequency bond-stretching modes driving PTE have not yet been significantly populated to interfere with the intrinsic negative expansion behavior. Crucially, to ensure data consistency and eliminate discrepancies between experimental and theoretical sources, all elastic descriptors (e.g., B, G, E) for all 324 materials were uniformly recalculated using the uMLIP of MatterSim. We constructed a primary feature space containing 10 physically motivated variables chosen to capture lattice stiffness, bonding characteristics, and structural topology: elastic moduli (B, G, E, ν), energetic properties (U_V), lattice parameters $(\widetilde{v_{\mathrm{A}}}, n, \phi)$, and atomic and phonon descriptors (χ, Θ_D). These primary features were recursively combined up to a complexity level of 3 using a comprehensive set of mathematical operators, $S = \{+, -, \times, /, \exp, \log, \sqrt{}, |\cdot|, (\cdot)^2, (\cdot)^3\}$, generating a candidate feature space exceeding 10^6 dimensions. The most relevant descriptors were identified through iterative sure independence screening (SIS) followed by L_0-regularized sparsification. Among the top-ranked candidates, the dimensionless ratio $\xi = G/(U_V/n)$ was identified as the optimal descriptor due to its superior balance of classification accuracy and physical interpretability. To assess the model's robustness, we performed stratified 5-fold cross-validation. The model achieved a mean accuracy of 96.28% (±3.96%) and a mean Area Under the Curve (AUC) of 0.9889 (±0.0248), demonstrating excellent generalizability. The final classification boundary, $\xi_c = 2.69$, which separates the NTE ($\xi < \xi_c$) and PTE ($\xi > \xi_c$) regions, was determined from the full cubic training dataset. The fixed boundary was subsequently applied to the non-cubic OOD subset without refitting.

Supporting Information Available

This information is available free of charge via the Internet at http://pubs.acs.org.

- Supplementary notes, tables and figures for the explanation and physical interpretation of the shear-bond descriptor, scaling relationship between thermal expansion and mechanical descriptors, validation of the universal machine-learning interatomic potential using isotropic QHA and tensor-aware anisotropic Grüneisen calculations, benchmark comparisons between MatterSim and DFT-QHA, anisotropic thermal-expansion comparisons with published data, analysis of macroscopic Grüneisen parameters, data selection and distribution analysis for the cubic training and non-cubic out-of-domain sets, tabulated summary of primary features and top-ranked SISSO descriptors, full thermal-expansion dataset with literature provenance, descriptor calculations for amorphous materials, polymers, zeolites, molecular crystals and MOFs, experimental synthesis and synchrotron X-ray diffraction details, summary of newly predicted and experimentally verified NTE materials, classification maps for PTE and NTE materials, high-throughput thermal-expansion benchmarks, and supporting references.

Acknowledgements

The authors acknowledge the financial support of the National Natural Science Foundation of China (Nos. 12572126, 22471246), the Natural Science Foundation of the Higher Education

Institutions of Jiangsu Province, China (No. 25KJB120008). The SXRD experiments were performed at the BL02B2 of SPring-8 with the approval of the Japan Synchrotron Radiation Research Institute (JASRI, proposal Nos. 2025A1945 and 2025A1927). The work was carried out at the National Supercomputer Center in Tianjin, and the calculations were performed on TianHe-1(A).

Conflicts of interest

There are no conflicts to declare.

Author contributions

G.C and S.T contributed equally to this work.

Codes availability

The codes and input scripts used within this work are available from the corresponding authors upon reasonable request.

Data availability

The data within this paper and other findings of this study are available from the corresponding authors upon reasonable request. The NTE materials discovered in this work is available at NTE materials database (NTEdb).

References

(1) Barron, T.; Collins, J.; White, G. Thermal expansion of solids at low temperatures. *Adv. Phys.* **1980**, *29*, 609–730.

(2) Roy, R.; Agrawal, D. K.; McKinstry, H. A. Very low thermal expansion coefficient materials. *Annu. Rev. Mater. Sci.* **1989**, *19*, 59–81.

(3) Sleight, A. Zero-expansion plan. *Nature* **2003**, *425*, 674–676.

(4) Fisher, D. J. *Negative thermal expansion materials*; Materials Research Forum LLC, 2018.

(5) Mary, T. A.; Evans, J. S. O.; Vogt, T.; Sleight, A. Negative thermal expansion from 0.3 to 1050 Kelvin in ZrW_2O_8. *Science* **1996**, *272*, 90–92.

(6) Ernst, G.; Broholm, C.; Kowach, G.; Ramirez, A. Phonon density of states and negative thermal expansion in ZrW_2O_8. *Nature* **1998**, *396*, 147–149.

(7) Shi, N.; Song, Y.; Xing, X.; Chen, J. Negative thermal expansion in framework structure materials. *Coord. Chem. Rev.* **2021**, *449*, 214204.

(8) Dove, M. T.; Fang, H. Negative thermal expansion and associated anomalous physical properties: review of the lattice dynamics theoretical foundation. *Rep. Prog. Phys.* **2016**, *79*, 066503.

(9) Li, Q.; Lin, K.; Liu, Z.; Hu, L.; Cao, Y.; Chen, J.; Xing, X. Chemical diversity for tailoring negative thermal expansion. *Chem. Rev.* **2022**, *122*, 8438–8486.

(10) Yang, H.; Xu, P.; Al-Maythalony, B. A.; Huang, Y.; Xu, M.; Hua, Y.; Zhang, W.; Wang, X.; Cui, S.; Zhu, H.; Xu, B. Negative-thermal-expansion particles enable high-performance and ultradurable thermoelectric modules. *Sci. Adv.* **2026**, *12*, eaed3783.

(11) Sougleridis, I. I.; Brun, M.; Baldi, A.; Carta, G. Microstructured tunable media with giant negative and positive thermal expansion. *J. Mech. Phys. Solids* **2025**, 106373.

(12) Xia, X.; Spadaccini, C. M.; Greer, J. R. Responsive materials architected in space and time. *Nat. Rev. Mater.* **2022**, *7*, 683–701.

(13) Lakes, R. Cellular solid structures with unbounded thermal expansion. *J. Mater. Sci. Lett.* **1996**, *15*, 475–477.

(14) Yarali, E.; Mirzaali, M. J.; Ghalayaniesfahani, A.; Accardo, A.; Diaz-Payno, P. J.; Zadpoor, A. A. 4D printing for biomedical applications. *Adv. Mater.* **2024**, *36*, 2402301.

(15) Ni, X.; Guo, X.; Li, J.; Huang, Y.; Zhang, Y.; Rogers, J. A. 2D mechanical metamaterials with widely tunable unusual modes of thermal expansion. *Adv. Mater.* **2019**, *31*, 1905405.

(16) Yang, S.; Yang, D.-B.; Ning, Y.; Zhang, Y.; Kikkawa, J. M.; Saven, J. G.; Murray, C. B. Super-expansive thermo-reversible interstitial solid solution of nanocrystal superlattices with mesogens. *Nat. Mater.* **2025**, 1–8.

(17) Gao, Q.; Jiao, Y.; Sprenger, J. A.; Finze, M.; Sanson, A.; Sun, Q.; Liang, E.; Chen, J. Critical role of nonrigid unit and spiral acoustical modes in designing colossal negative thermal expansion. *J. Am. Chem. Soc.* **2024**, *146*, 21710–21720.

(18) Gao, Q.; Wang, J.; Sanson, A.; Sun, Q.; Liang, E.; Xing, X.; Chen, J. Discovering large isotropic negative thermal expansion in framework compound $AgB(CN)_4$ via the concept of average atomic volume. *J. Am. Chem. Soc.* **2020**, *142*, 6935–6939.

(19) Mounet, N.; Marzari, N. First-principles determination of the structural, vibrational and thermodynamic properties of diamond, graphite, and derivatives. *Phys. Rev. B* **2005**, *71*, 205214.

(20) Jain, A.; Ong, S. P.; Hautier, G.; Chen, W.; Richards, W. D.; Dacek, S.; Cholia, S.; Gunter, D.; Skinner, D.; Ceder, G.; Persson, K. A. Commentary: The Materials Project: A materials genome approach to accelerating materials innovation. *APL Mater.* **2013**, *1*, 011002.

(21) Merchant, A.; Batzner, S.; Schoenholz, S. S.; Aykol, M.; Cheon, G.; Cubuk, E. D. Scaling deep learning for materials discovery. *Nature* **2023**, *624*, 80–85.

(22) Tian, S.; Zhou, K.; Yin, W.; Liu, Y. Machine learning enables the discovery of 2D Invar and anti-Invar monolayers. *Nat. Commun.* **2024**, *15*, 6977.

(23) Rao, Z. et al. Machine learning–enabled high-entropy alloy discovery. *Science* **2022**, *378*, 78–85.

(24) Wang, T.; Hu, J.; Ouyang, R.; Wang, Y.; Huang, Y.; Hu, S.; Li, W.-X. Nature of metal-support interaction for metal catalysts on oxide supports. *Science* **2024**, *386*, 915–920.

(25) Ouyang, R.; Curtarolo, S.; Ahmetcik, E.; Scheffler, M.; Ghiringhelli, L. M. SISSO: A compressed-sensing method for identifying the best low-dimensional descriptor in an immensity of offered candidates. *Phys. Rev. Mater.* **2018**, *2*, 083802.

(26) Cai, Y.; Wang, C.; Yuan, H.; Guo, Y.; Cho, J.-H.; Xing, X.; Jia, Y. Exploring negative thermal expansion materials with bulk framework structures and their relevant scaling relationships through multi-step machine learning. *Mater. Horiz.* **2024**, *11*, 2914–2925.

(27) Zhang, Y.; Mu, H.; Cai, Y.; Wang, X.; Zhou, K.; Tian, F.; Fu, Y.; Zhang, L. Evaluating thermal expansion in fluorides and oxides: Machine learning predictions with connectivity descriptors. *Chin. Phys. B* **2023**, *32*, 056302.

(28) Gao, Z.; Zhou, X.; Xu, M.; Xu, Y.; Tian, F. High-throughput screening anisotropic negative thermal expansion framework materials. *Acta Mater.* **2025**, *300*, 121493.

(29) Song, Y.; Shi, N.; Deng, S.; Xing, X.; Chen, J. Negative thermal expansion in magnetic materials. *Prog. Mater Sci.* **2021**, *121*, 100835.

(30) Xu, M.; Gao, Q.; Qiao, Y.; Zhao, K.; Sanson, A.; Sun, Q.; Wang, C.; Venier, A.; d'Acapito, F.; Tucker, M.; Song, Y. S.; Zhou, C.; Xing, X.; Chen, J. Quantitative Role of Phonons and Elasticity in Tuning Uniaxial Negative Thermal Expansion of MZr_2 (M= Fe, Co, and Ni). *Phys. Rev. Lett.* **2025**, *135*, 166101.

(31) Barron, T.; Collins, J.; White, G. Thermal expansion of solids at low temperatures. *Adv. Phys.* **1980**, *29*, 609–730.

(32) Pozzo, M.; Alfe, D.; Lacovig, P.; Hofmann, P.; Lizzit, S.; Baraldi, A. Thermal expansion of supported and freestanding graphene: lattice constant versus interatomic distance. *Phys. Rev. Lett.* **2011**, *106*, 135501.

(33) Jin, R.; Yuan, X.; Gao, E. Atomic stiffness for bulk modulus prediction and high-throughput screening of ultraincompressible crystals. *Nat. Commun.* **2023**, *14*, 4258.

(34) Miao, L.; Yuan, X.; Tang, C.; Chen, C.; Gao, E. A large atomic partition model for materials discovery. *Extreme Mech. Lett.* **2024**, *73*, 102262.

(35) Heine, V.; Welche, P. R.; Dove, M. T. Geometrical origin and theory of negative thermal expansion in framework structures. *J. Am. Ceram. Soc.* **1999**, *82*, 1793–1802.

(36) Pugh, S. Relations between the elastic moduli and the plastic properties of polycrystalline pure metals. *Philos. Mag.* **1954**, *45*, 823–843.

(37) NTEdb: NTE Materials Database. 2026; `https://www.ntedb.com`, accessed May 22, 2026.

(38) Loew, A.; Sun, D.; Wang, H.-C.; Botti, S.; Marques, M. A. Universal machine learning interatomic potentials are ready for phonons. *npj Comput. Mater.* **2025**, *11*, 178.

(39) Li, J. et al. Probing the Limit of Heat Transfer in Inorganic Crystals with Deep Learning. *arXiv preprint arXiv:2503.11568* **2025**,

(40) Cignarella, C.; Bastonero, L.; Monacelli, L.; Marzari, N. Extreme Anharmonicity and Thermal Contraction of One-Dimensional Wires. *Nano Lett.* **2025**, *25*, 15919–15926.

(41) Zhong, Y.; Wang, R.; Gong, X.; Xiang, H. A universal spin–orbit-coupled Hamiltonian model for accelerated quantum material discovery. *Nat. Mach. Intell.* **2026**, 1–12.

(42) Yu, H.; Zhong, Y.; Hong, L.; Xu, C.; Ren, W.; Gong, X.; Xiang, H. Spin-dependent graph neural network potential for magnetic materials. *Phys. Rev. B* **2024**, *109*, 144426.

(43) Zhong, Y.; Yu, H.; Su, M.; Gong, X.; Xiang, H. Transferable equivariant graph neural networks for the Hamiltonians of molecules and solids. *npj Comput. Mater.* **2023**, *9*, 182.

(44) Togo, A.; Tanaka, I. First Principles Phonon Calculations in Materials Science. *Scripta Materialia* **2015**, *108*, 1–5.

(45) Ritz, E. T.; Li, S. J.; Benedek, N. A. Thermal expansion in insulating solids from first principles. *J. Appl. Phys.* **2019**, *126*, 171102.

(46) Yang, H. et al. MatterSim: A deep learning atomistic model across elements, temperatures and pressures. *arXiv preprint arXiv:2405.04967* **2024**,

(47) Kresse, G.; Furthmüller, J. Efficiency of ab-initio total energy calculations for metals and semiconductors using a plane-wave basis set. *Comput. Mater. Sci* **1996**, *6*, 15–50.

(48) Kresse, G.; Furthmüller, J. Efficient iterative schemes for ab initio total-energy calculations using a plane-wave basis set. *Phys. Rev. B* **1996**, *54*, 11169.

(49) Blöchl, P. E. Projector augmented-wave method. *Phys. Rev. B* **1994**, *50*, 17953.

(50) Perdew, J. P.; Burke, K.; Ernzerhof, M. Generalized gradient approximation made simple. *Phys. Rev. Lett.* **1996**, *77*, 3865.

(51) Wang, V.; Xu, N.; Liu, J.-C.; Tang, G.; Geng, W.-T. VASPKIT: A user-friendly interface facilitating high-throughput computing and analysis using VASP code. *Comput. Phys. Commun.* **2021**, *267*, 108033.

(52) Zimmermann, N. E. R.; Jain, A. Local Structure Order Parameters and Site Fingerprints for Quantification of Coordination Environment and Crystal Structure Similarity. *RSC Adv.* **2020**, *10*, 6063–6081.

(53) Ong, S. P.; Richards, W. D.; Jain, A.; Hautier, G.; Kocher, M.; Cholia, S.; Gunter, D.; Chevrier, V. L.; Persson, K. A.; Ceder, G. Python Materials Genomics (Pymatgen): A Robust, Open-Source Python Library for Materials Analysis. *Comput. Mater. Sci* **2013**, *68*, 314–319.

(54) Kittel, C.; McEuen, P. *Introduction to Solid State Physics*; John Wiley & Sons, 2018.

Table of Contents Graphic